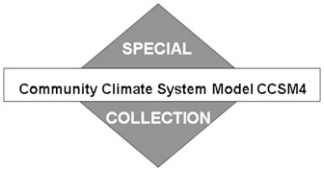

The Mean Climate of the Community Atmosphere Model (CAM4) in Forced SST and Fully Coupled Experiments

RICHARD B. NEALE, JADWIGA RICHTER, SUNGSU PARK, AND PETER H. LAURITZEN

National Center for Atmospheric Research, Boulder, Colorado

STEPHEN J. VAVRUS

Center for Climatic Research, University of Wisconsin—Madison, Madison, Wisconsin

PHILIP J. RASCH

Pacific Northwest National Laboratory, Richland, Washington

MINGHUA ZHANG

School of Marine and Atmospheric Sciences, Stony Brook University, State University of New York, Stony Brook, New York

(Manuscript received 24 April 2012, in final form 3 January 2013)

ABSTRACT

The Community Atmosphere Model, version 4 (CAM4), was released as part of the Community Climate System Model, version 4 (CCSM4). The finite volume (FV) dynamical core is now the default because of its superior transport and conservation properties. Deep convection parameterization changes include a dilute plume calculation of convective available potential energy (CAPE) and the introduction of convective momentum transport (CMT). An additional cloud fraction calculation is now performed following macrophysical state updates to provide improved thermodynamic consistency. A freeze-drying modification is further made to the cloud fraction calculation in very dry environments (e.g., the Arctic), where cloud fraction and cloud water values were often inconsistent in CAM3. In CAM4 the FV dynamical core further degrades the excessive trade-wind simulation, but reduces zonal stress errors at higher latitudes. Plume dilution alleviates much of the midtropospheric tropical dry biases and reduces the persistent monsoon precipitation biases over the Arabian Peninsula and the southern Indian Ocean. CMT reduces much of the excessive trade-wind biases in eastern ocean basins. CAM4 shows a global reduction in cloud fraction compared to CAM3, primarily as a result of the freeze-drying and improved cloud fraction equilibrium modifications. Regional climate feature improvements include the propagation of stationary waves from the Pacific into midlatitudes and the seasonal frequency of Northern Hemisphere blocking events. A 1° versus 2° horizontal resolution of the FV dynamical core exhibits superior improvements in regional climate features of precipitation and surface stress. Improvements in the fully coupled mean climate between CAM3 and CAM4 are also more substantial than in forced sea surface temperature (SST) simulations.

1. Introduction

The Community Atmosphere Model, version 4 (CAM4), is the seventh generation atmospheric general circulation model (AGCM) developed with significant community collaboration at the National Center for Atmospheric Research (NCAR). CAM4 comprises the atmosphere component of the Community Climate System Model, version 4 (CCSM4; Gent et al. 2011). For the first time CAM is fully integrated into the coupled CCSM4 system using either data or thermodynamic components of surface models for forced SST and Slab Ocean Model (SOM) runs or interactive versions of the same surface models for full climate system experiments. The same surface components updated in CCSM4 are also included, when appropriate, in CAM4 simulations [e.g., Community Land Model (CLM) and Los Alamos Sea

Corresponding author address: Dr. Richard B. Neale, National Center for Atmospheric Research, P.O. Box 3000, Boulder, CO 80307.
E-mail: rneale@ucar.edu

DOI: 10.1175/JCLI-D-12-00236.1

Ice Model (CICE); Gent et al. 2011]. CAM4 includes moderate changes in model configuration compared to CAM3 (Collins et al. 2006a), but exhibits significant changes and improvements in climate compared to CAM3. This article summarizes the improvements seen in the seasonally varying mean atmospheric climate of prescribed-SST and fully coupled simulations. The dominant changes made to the model configuration involve the parameterization of deep convection. These changes have a significant impact on improving the pattern of long-standard tropical errors such as El Niño–Southern Oscillation (ENSO; Deser et al. 2012) and the Madden–Julian oscillation (MJO; Subramanian et al. 2011). A further change for CAM4 has been to increase the horizontal resolution of the model from T85 (nominally 1.4° at the equator) to a regular 1° grid with the finite volume (FV) dynamical core. In addition to the default version of CAM4 using the FV dynamical core (CAM4-FV), an alternate dynamical core using a nominally unstructured grid is also available in CAM4. This is the first time an unstructured grid has been made available in CAM and is based upon High-Order Method Model Environment (HOMME; Dennis et al. 2012) spectral element (SE) methods. Initial simulations using this dynamical core option (CAM4-SE) demonstrate comparable skill to CAM4-FV (Evans et al. 2013; Mishra et al. 2011).

This paper documents changes to physical parameterization formulations in CAM4 and highlights their dominant impact in SST-forced and fully coupled experiments. Section 2 describes the changes made to physics and dynamics formulations since CAM3. Section 3 presents a summary of model simulations examined and observational data used. Section 4 summarizes explicit climate changes related to model changes between CAM3 and CAM4, and section 5 details improvements in more general aspects of the model climate in prescribed-SST and fully coupled experiments. Conclusions are presented in section 6.

2. Overview of model formulation and dataset changes

A number of modifications have been implemented in CAM4, the most impactful of which are summarized below. A more comprehensive description of CAM4 can be found in Neale et al. (2011).

a. Dynamical core and resolution changes

The FV dynamical core, available as an option in CAM3 (Lin and Rood 1996; Lin 2004), is now the default option in CAM4. This is primarily because of the improved tracer transport capabilities highlighted in CAM3 age-of-air experiments (Rasch et al. 2006) and their relevance to a growing range of chemistry applications [e.g., Model for Ozone and Related Chemical Tracers (MOZART); Emmons et al. 2009]. Initial CAM4 development experiments focused on a 1.9° latitude by 2.5° longitude resolution, but idealized aqua-planet experiments show that a resolution of $0.9° \times 1.25°$ is required in order to provide an equivalent resolution to the CAM3 T85 spectral core configuration (Williamson and Olson 2007). Therefore, $0.9° \times 1.25°$ is the default resolution for most CAM4 applications. The $1.9° \times 2.5°$ resolution is still used for more computationally intensive applications such as the Whole Atmosphere Community Climate Model (WACCM; http://www.cesm.ucar.edu/working_groups/WACCM/) and CAM chemistry (e.g., Lamarque et al. 2012). For CAM4 the default number of levels remains at 26 as a result of an undesirable nonconvergent response from boundary layer and shallow convection interactions when levels were significantly increased (Williamson 2013).

Because of the presence of grid-scale noise and excessive polar night jets, two new filtering/diffusion operators have been implemented in CAM4-FV (Lauritzen et al. 2011). First, a fourth-order divergence damping operator has been added to optionally replace the second-order version used in CAM3-FV. In general, it provides a more scale selective dissipation of divergent modes (Whitehead et al. 2011) that can generate grid-scale noise in CAM-FV if not damped properly. Second, a Laplacian-type damping operator has been implemented to increase the explicit momentum dissipation in the top-of-atmosphere sponge layers. This helps control the excessive polar night jets that have been observed in higher-resolution CAM-FV simulations. Further minor modifications harmonize the critical Froude number value between CAM and WACCM. The critical Froude number controls the initiation of orographic gravity wave generation and breaking in CAM, and the increase in its value from 0.5 to 1.0 has only a minor climate impact on the CAM simulation.

b. Deep convection

The application of the deep convection parameterization in CAM4 continues to be based upon the bulk mass-flux scheme of Zhang and McFarlane (1995; ZM scheme). One addition and one significant modification have been made to the ZM scheme and are summarized below.

1) CONVECTIVE PLUME DILUTION

In CAM3, the closure of the ZM scheme uses a calculation of convective available potential energy (CAPE) based on a reference ascending air parcel that does not entrain with its grid-mean environment. This undilute

CAPE (UCAPE) approximation exhibits limited sensitivity to free-troposphere humidity variations and excessive sensitivity to near-surface humidity and temperature variations (Zhang 2009). As such, the deep convective response in CAM3 was strongly coupled to diurnal variations over land and SST variations over ocean (Williamson and Olson 2007). To address these shortcomings the UCAPE calculation was replaced by a dilute CAPE (DCAPE) calculation based on the mixing models of Raymond and Blyth (1986, 1992). The calculation of UCAPE based on the conservation of moist potential temperature θ_e is replaced with a mixing model based on the conservation of moist entropy including liquid water.

The conserved variable is

$$s = (C_{\mathrm{pd}} + q_T C_L)\ln\left(\frac{T}{T_R}\right) - R_D \ln\left(\frac{p_D}{p_R}\right) + L\frac{q_v}{T} - q_v R_v \ln\left(\frac{q_v}{q_s}\right), \quad (1)$$

where C_{pd} and C_L are the specific heat at constant pressure for dry air and the specific heat for liquid water respectively, R_D and R_v are the dry air and water vapor gas constants respectively, L is the latent heat of vaporization, T is absolute temperature, and p_D is the partial pressure of dry air. Here, q_v, q_T, and q_s are the vapor, total water, and saturated mixing ratios respectively. Reference quantities are $T_R = 273.15$ K and $p_R = 1000$ hPa. While this quantity is conserved in reversible adiabatic processes it is continually mixed with the equivalent value of moist entropy in the environment, and s_E according to a constant entrainment rate ϵ such that

$$s^k = (1-\epsilon)s^{k+1} + \epsilon s_E^{k+1}, \quad (2)$$

where k is model level increasing downward. A constant value of $\epsilon = 1\ \mathrm{km}^{-1}$ is used globally, which is a typical value of entrainment used to represent shallow convecting clouds. Larger values of ϵ tend to inhibit deep convection and moisten the lower troposphere too much, while higher values exhibit a response that retains the lack of moisture sensitivity seen in CAM3. The vertical profiles of T, q_v, and q_T in the assumed convecting parcels are derived from a simple inversion of s and are then used for the calculation of buoyancy, total CAPE, and triggering CAPE as in CAM3. The DCAPE calculation was first used in simulations using the interim CAM3.5 release (Neale et al. 2008; Gent et al. 2010).

2) Convective momentum transport

Subgrid-scale convective momentum transport (CMT) has been added to the existing deep convection parameterization following Richter and Rasch (2008) and the methodology of Gregory et al. (1997). The subgrid-scale convective transport of momentum can be cast in the same manner as for humidity and static energy. Expressing the grid-mean horizontal velocity vector $\mathbf{V}$ tendency due to deep convection transport following Kershaw and Gregory (1997) gives

$$\left(\frac{\partial \mathbf{V}}{\partial t}\right)_{\mathrm{cu}} = -\frac{1}{\rho}\frac{\partial}{\partial z}(M_u\mathbf{V}_u + M_d\mathbf{V}_d - M_c\mathbf{V}), \quad (3)$$

where the cumulus mass flux is $M_c = M_u + M_d$. Neglecting the contribution from the environment, the updraft and downdraft budget equation can similarly be written as

$$-\frac{\partial}{\partial z}(M_u\mathbf{V}_u) = E_u\mathbf{V} - D_u\mathbf{V}_u + \mathbf{P}_G^u \quad \text{and} \quad (4)$$

$$-\frac{\partial}{\partial z}(M_d\mathbf{V}_d) = E_d\mathbf{V} + \mathbf{P}_G^d, \quad (5)$$

where $\mathbf{P}_G^u$ and $\mathbf{P}_G^d$ are the updraft and downdraft pressure gradient sink terms parameterized from Gregory et al. (1997) as

$$\mathbf{P}_G^u = -C_u M_u \frac{\partial \mathbf{V}}{\partial z} \quad \text{and} \quad (6)$$

$$\mathbf{P}_G^d = -C_d M_d \frac{\partial \mathbf{V}}{\partial z}. \quad (7)$$

Note that C_u and C_d are tunable parameters. In the CAM4 implementation we use $C_u = C_d = 0.4$. The value of C_u and C_d control the strength of convective momentum transport. As these coefficients increase so do the pressure gradient terms and convective momentum transport decreases.

c. Cloud fraction

1) Freeze drying

In CAM3 polar wintertime cloud fraction was severely overestimated when compared with existing estimates available prior to the availability of *CloudSat* data. This overestimation was diagnosed to be acute during Northern Hemisphere winter. The relative humidity-based cloud fraction scheme of Zhang et al. (2003) allowed high cloud fractions to be produced even in the presence of very low values of ambient specific humidity q_v. A remedy to this feature is implemented into CAM4 following Vavrus and Waliser (2008). During periods of very dry conditions in the lower troposphere (at pressures below 700 hPa) a modification is made to the relative humidity cloud fraction calculation C_{low}^0:

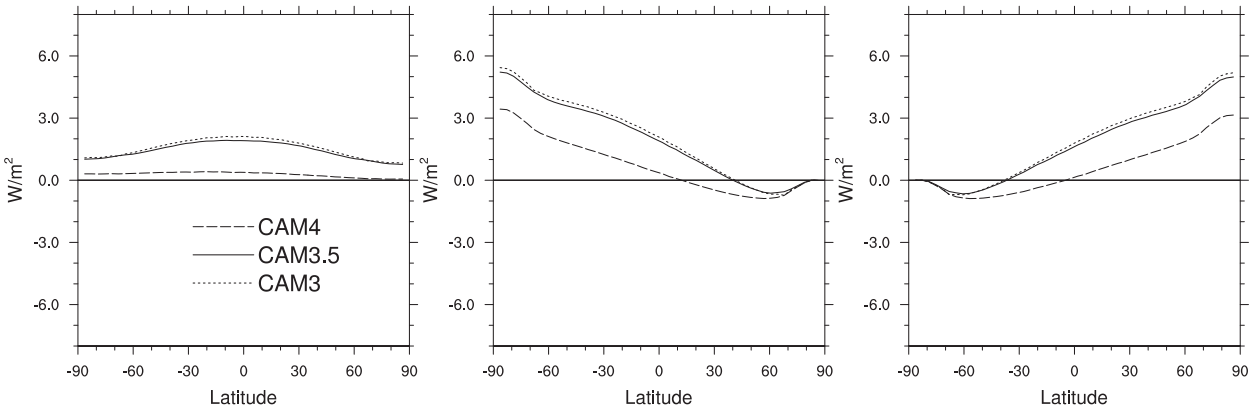

FIG. 1. Differences in zonal distribution of solar insolation between CAM3 and CAM4 compared to CERES-EBAF (2000–10) estimate of the (left) annual, (middle) DJF, and (right) JJA average.

$$C_{\text{low}} = C^0_{\text{low}} \max\left[0.15, \min\left(1, \frac{q_v}{0.003}\right)\right]. \qquad (8)$$

This adjustment in dry conditions significantly moderates the wintertime Arctic cloud fraction and results in a more accurate seasonal variation in low cloud cover (Vavrus and Waliser 2008).

2) CONSISTENT CLOUD FRACTION CALCULATION

To prevent inconsistent values of total cloud fraction and condensate being passed to the radiation parameterization in CAM4, a second updated cloud fraction calculation is performed. Cloud fraction, and therefore relative humidity, is now thermodynamically consistent with condensate values on entry to the radiation parameterization. This vastly reduces the frequency of empty clouds seen in the CAM3, where cloud condensate was zero and yet cloud had been diagnosed to exist as a result of an inconsistent relative humidity. This modification greatly reduced low cloud fraction over Asia and North America during wintertime, and by enhancing upward longwave radiation emitted from the surface to the free atmosphere, positive biases of near-surface air temperature were also substantially reduced. These had been long-standing biases in CAM3. In addition, variation of cloud fraction and in-cloud condensate becomes more consistent as detailed in Park et al. (2012, unpublished manuscript).

3) AEROSOL CHANGES

New consistent gridded emissions of reactive gases and aerosols for use in chemistry model simulations and needed by climate models for phase 5 of the Coupled Model Intercomparison Project (CMIP5) in support of the Intergovernmental Panel on Climate Change (IPCC) Fifth Assessment Report (AR5) are now available using the tropospheric MOZART (TROP-MOZART) framework in CAM (Lamarque et al. 2010). These datasets are used to drive the twentieth-century historical simulations analyzed here.

4) OTHER CHANGES

There have been a number of other changes between CAM3 and CAM4 that have an impact on the climate simulations. Chief among these is the specification of a new solar irradiance dataset. Figure 1 shows the evolution of the seasonal change in the distribution of solar insolation at the top of the model. From CAM3 to CAM3.5 the reference orbital year was updated to 1990 from 1950 to be more accurate for late twentieth-century simulations. This had a global impact of $+0.2\ \text{W m}^{-2}$. A larger change to CAM4 was the transition to the more recent Kopp and Lean (2011) total solar irradiance dataset based on the Total Irradiance Monitor (TIM) on the National Aeronautics and Space Administration's (NASA) Solar Radiation and Climate Experiment (SORCE). This new estimate of total solar irradiance was around $1365.4\ \text{W m}^{-2}$, more than $4.6\ \text{W m}^{-2}$ lower than the dataset used in CAM3. This translates to a reduction in top of atmosphere average incoming insolation of $1.1\ \text{W m}^{-2}$ in CAM4, which is concentrated at summertime high latitudes.

Finally, there was an effective reduction made in the fall velocity of ice cloud particles at the lower 2° resolution in CAM4. This was to facilitate the development of the WACCM4 in order to provide a more realistic source of upper-tropospheric water vapor that could be transported into the lower stratosphere and alleviate significant dry biases there.

TABLE 1. Summary details of the CAM and CCSM experiments analyzed using CAM3, CAM4, and intermediate development model versions.

Name	Horizontal resolution	Description	SST	Analysis period
CAM3	T42	Spectral low resolution	AMIP	1981–2000
CAM3	T85	Spectral high resolution	AMIP	1981–2000
CAM3	2°	FV low resolution	AMIP	1980–99
CAM3-DIL	2°	FV + CAPE dilution	AMIP	1980–99
CAM3-CMT	2°	FV + CMT	AMIP	1980–99
CAM3-CONV	2°	FV + convective changes (CMT + DIL)	AMIP	1980–99
CAM3.5	2°	FV-CONV + freeze-drying + cloud fraction update; interim CAM release (Gent et al. 2010)	AMIP	1979–2005
CAM4	2°	FV low resolution	AMIP	1981–2000
CAM4	1°	FV high resolution	AMIP	1981–2000
CCSM3	T85	Spectral high resolution	Coupled	1970–99
CCSM4	2°	FV low resolution	Coupled	1970–99
CCSM4	1°	FV high resolution	Coupled	1970–99

3. Experiment and observational data

a. Model simulations

Two different types of integrations are analyzed; prescribed SST (CAM) and fully coupled (CCSM) experiments. All experiments are summarized in Table 1.

1) FORCED EXPERIMENTS

The configuration for CAM experiments consists of fully interactive atmosphere and CLM components. A data ocean model is used that allows prescribed SSTs and a version of the CICE in thermodynamic-only mode where ice extent is prescribed from observations and ice thickness is specified. The prescribed SSTs and sea ice properties are derived from the Atmosphere Model Intercomparison Project (AMIP; Taylor et al. 2001), whereby linearly interpolated daily values are obtained from adjusted monthly average datasets that maintain the observed monthly means as near as possible. These experiments begin in 1979 and extend into 2005.

2) FULLY COUPLED EXPERIMENTS

More comprehensive experiments are analyzed where a fully interactive version of the Parallel Ocean Program (POP) model and CICE are used in experiments. These experiments begin from a fully interactive coupled model integration that has a near-zero energy imbalance at the top of the atmosphere and has been subject to a multicentennial spinup period when subject to preindustrial (circa 1850) major climate forcings.

b. Observational data

Comparisons are made to standard observational satellite, in situ and reanalysis datasets including the 15-yr European Center for Medium-Range Weather Forecasts (ECMWF) Re-Analysis (ERA-15; Gibson et al. 1997), 40-yr ECMWF Re-Analysis (ERA-40; Uppala et al. 2005), ECMWF Interim Re-Analysis (ERA-Interim; Dee et al. 2011), the NASA Modern-Era Retrospective Analysis for Research and Applications (MERRA; Rienecker et al. 2011), the Japanese 25-yr Reanalysis (JRA-25; Onogi et al. 2007), and the National Centers for Environmental Prediction–Department of Energy (NCEP–DOE) AMIP II Reanalysis (R-2; Kanamitsu et al. 2002). NASA Clouds and the Earth's Radiant Energy System, energy balanced and filled (CERES-EBAF; Loeb et al. 2009) and the Earth Radiation Budget Experiment (ERBE; Barkstrom and Hall 1982) are used for top of atmosphere radiative fields. For precipitation, we compare with the Global Precipitation Climatology Project (GPCP; Adler et al. 2003), the Climate Prediction Center (CPC) Merged Analysis of Precipitation (CMAP; Xie and Arkin 1997), and the Tropical Rainfall Measuring Mission (TRMM; Huffman et al. 2007) 3B42 product. For cloud quantities, we compare to a combined *CloudSat* spaceborne radar and *Cloud–Aerosol Lidar and Infrared Pathfinder Satellite Observations (CALIPSO)* spaceborne lidar cloud fraction dataset (*CloudSat*; Kay and Gettelman 2009) and the International Satellite Cloud Climatology Project (ISCCP; Schiffer and Rossow 1983) product, as well as, a gridded cloud climatology from ground-based observations (hereafter referred to as WARREN) described in Hahn and Warren (2007). For surface stresses, we compare with scatterometer winds from the European Remote-Sensing Satellites (ERS; Attema 1991). Finally, vertical profiles derived from radiosonde climatologies are provided from the rawindsonde observation (RAOBS) network (Peterson and Vose 1997). A comprehensive description of the observational datasets used is provided by NCAR's climate data guide (http://climatedataguide.ucar.edu/).

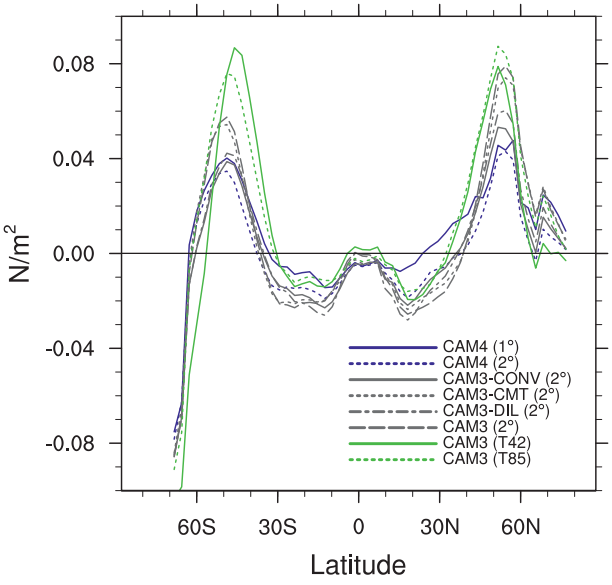

FIG. 2. Surface zonal stress (N m^{-2}), zonal average annual climate bias for CAM3 model versions (green), CAM3 development versions (gray), and CAM4 versions (blue) compared to *ERS-1* microwave scatterometer winds.

4. Dominant impacts of individual model changes

a. Finite volume dynamical core

Lauritzen et al. (2010) carefully compare the performance of CAM3 and CAM4 dynamical cores in dry idealized experiments. However, it is difficult to directly address the impact on the climate simulation of changing from the spectral to the FV dynamical core since we are comparing changes in numerics, algorithms, nominal resolution, and coupling to the physical parameterizations. Figure 2 shows the zonally averaged zonal surface stress biases comparing different dynamical core and development versions from CAM3 to CAM4. Different resolutions using the spectral dynamical core largely show more similarities with each other than with a 2° FV resolution. Excessive tropical seasonal monsoonal westerly flow biases are also present (not shown), but in the annual mean they are small and common to the two dynamical cores. Further poleward, to around 50°, FV surface stresses are consistently lower than those with the spectral dynamics. These changes lead to a detrimental overestimate of trade-wind strength in the subtopics in the FV transition models with a beneficial reduction in midlatitude westerlies poleward of around 40°, particularly in the Southern Hemisphere. The excessive easterly trade winds are consistent with a stronger Hadley circulation and intertropical convergence zone (ITCZ) seen with the inclusion of the FV dynamical core. These surface stress differences have strong implications for the coupled climate, which is discussed in a later section.

b. Dilute CAPE

The inclusion of DCAPE in the model has a significant impact on the partitioning of parameterized convective rainfall and resolved stratiform rainfall. Figure 3 shows that CAM3 has a stratiform contribution to tropical rainfall that is below 20% throughout most of the precipitating tropics. This would seem to be low given existing TRMM estimates ranging between 35% and 55% (Dai 2006). The largest impact on increasing the ratio of resolved tropical precipitation comes from the inclusion of DCAPE. This results in an increase in averaged resolved precipitation by around 6.5% and accounts for most of the increase in the resolved precipitation fraction ultimately seen in the CAM4 climate. Doubling resolution in CAM from 2° to 1° has the effect of increasing resolved precipitation by a few percent, but this is small compared to effects of DCAPE. Using an entraining parcel in CAM4 has the obvious impact of reducing the efficiency of UCAPE consumption and allowing resolved scale moistening to provide more of the tropical precipitation. Given the lack of explicit knowledge regarding the grid in the ZM formulation it cannot respond to increases in resolution, whereas the stratiform precipitation is able to respond to the more rapid saturation at finer grid scales and again contribute more to the tropical precipitation total, particularly in the central and east Pacific ITCZ which intensifies in CAM at 1°. A shift in the thermodynamic structure of the model is also seen with the inclusion of DCAPE. Figure 4 shows a lower-tropospheric dry bias and upper-tropospheric moist bias were prevalent in the precipitating tropics in CAM3. Williamson and Olson (2007) use forecast experiments to show the UCAPE approximation in CAM3 is much too stabilizing in the upper troposphere with a significant high bias in moist static energy. The consequences of this response are a rapid transition (within 1–2 days) to a dry and warm free troposphere. Including DCAPE provides a much more realistic vertical structure in the conditionally unstable tropics. Explicit entrainment in DCAPE throttles convection in an equilibrium time-mean sense since it is much more inefficient at stabilizing the troposphere. This behavior mixes more humidity into the boundary layer and lower troposphere as well as maintaining moisture levels in the upper troposphere. In terms of stability, moist static energy is decreased in the upper troposphere and increased in the lower troposphere, thus raising the level of the moist static energy minimum. The location of this level is crucial in the functioning of the ZM convection scheme as it determines

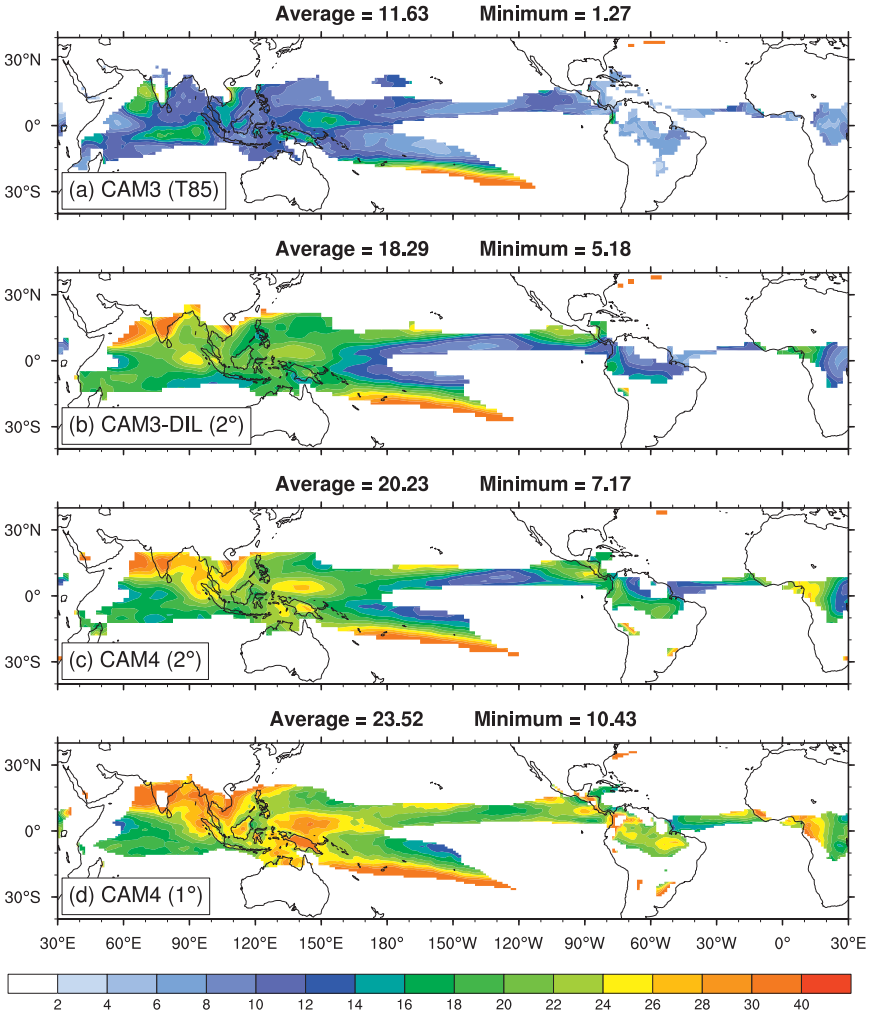

FIG. 3. Percentage of total precipitation from large-scale (resolved) processes for (a) CAM3 at T85, (b) CAM3-DIL at 2°, (c) CAM4 at 2°, and (d) CAM4 at 1°. Regions with precipitation less the 4 mm day^{-1} or large-scale fractions greater than 40% are excluded.

the first level at which both ascending convective plumes detrain and the downdraft plumes begin. A more realistic vertical structure is thus seen in CAM with the inclusion of DCAPE.

This vertical change in deep convection activity with DCAPE can be seen from the convective tendencies in Fig. 5. CAM3 ZM heating tendencies maximize in a deep layer of the ITCZ from 850 to 500 hPa and drying tendencies occur at all levels in the deep tropics with a maximum in the boundary layer. With the inclusion of DCAPE in CAM3-DIL, heating tendencies are reduced both in the boundary layer and the upper troposphere, consistent with a reduced convective precipitation contribution. More relevant to the tropical atmosphere is an increase in drying in the midtroposphere accompanied by decreases in the boundary layer drying and a marginal source of moisture in the upper troposphere. These moisture tendency shifts are consistent with the improved vertical moisture distribution seen in CAM3-DIL and CAM4.

c. *Convective momentum transport*

The incremental impact of including CMT is documented in Richter and Rasch (2008). They show a marginal improvement in the Hadley circulation with weakening of the northern upward branch and strengthening of the southern upward branch in December–February (DJF). The Hadley circulation and associated trade-wind changes are reflected in the zonally averaged surface stresses of Fig. 2 where the CAM3-CMT simulation has the greatest reduction in surface easterly stress bias of all the development model versions. However, the development model of CAM3-DIL appears to show the greatest reduction in the midlatitude surface westerly

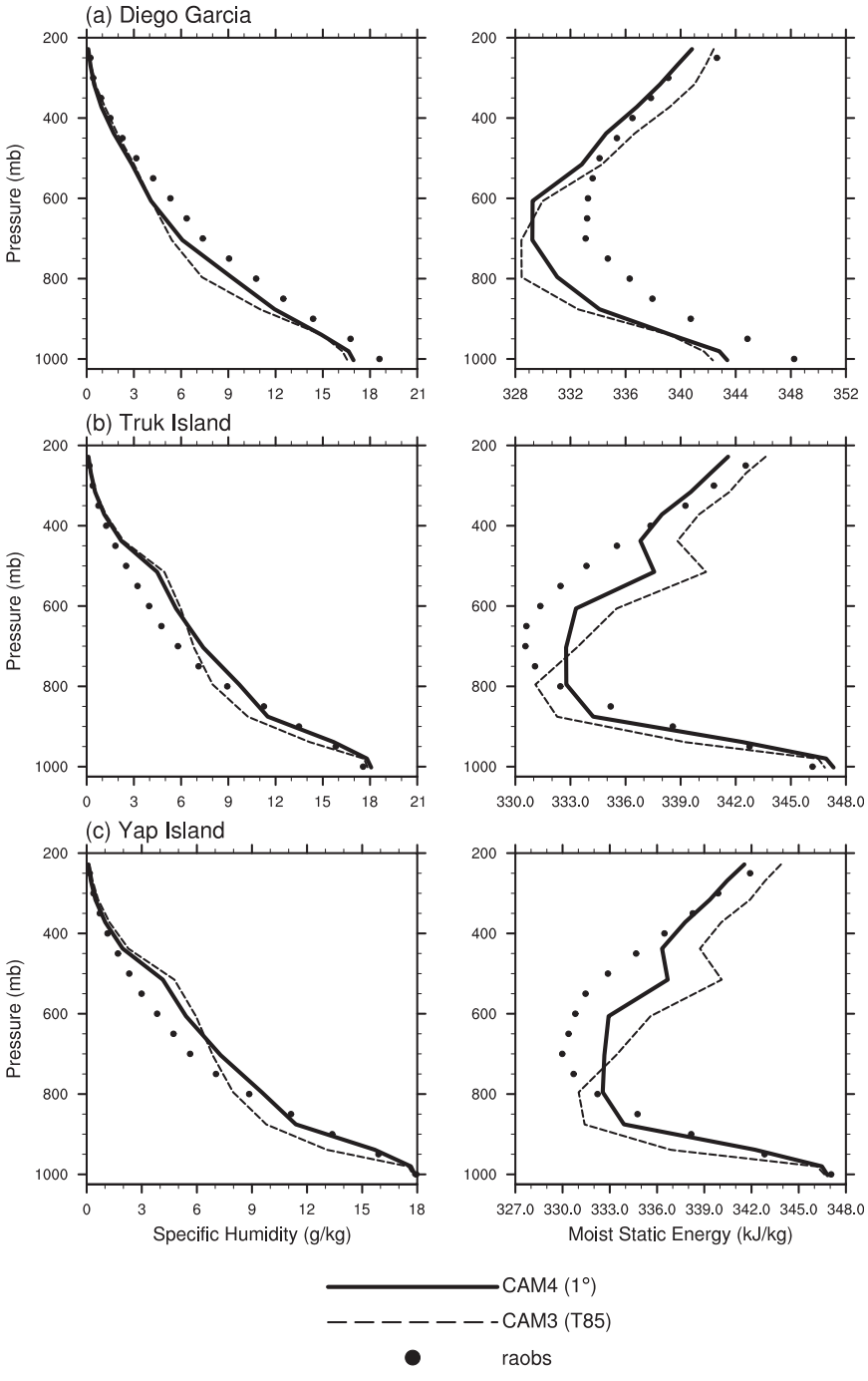

FIG. 4. (left) Vertical profiles of average July specific humidity (g kg^{-1}) and (right) moist static energy (kJ kg^{-1}) for RAOBS, and CAM3 T85 and CAM4 1° simulations.

stresses, and represents the largest part of the improvements between CAM3 and CAM4 resulting from a physics change. These improvements in high-latitude stress are identified in response to more realistic western Pacific tropical heating locations and stationary wave response in the Southern Hemisphere in particular. As with the DCAPE and CMT changes working in concert to enhance the tropical intraseasonal variability (Neale et al. 2008), they also combine to have a further positive impact on reducing the westerly stresses in the Northern Hemisphere in the CAM3-CONV development model simulation.

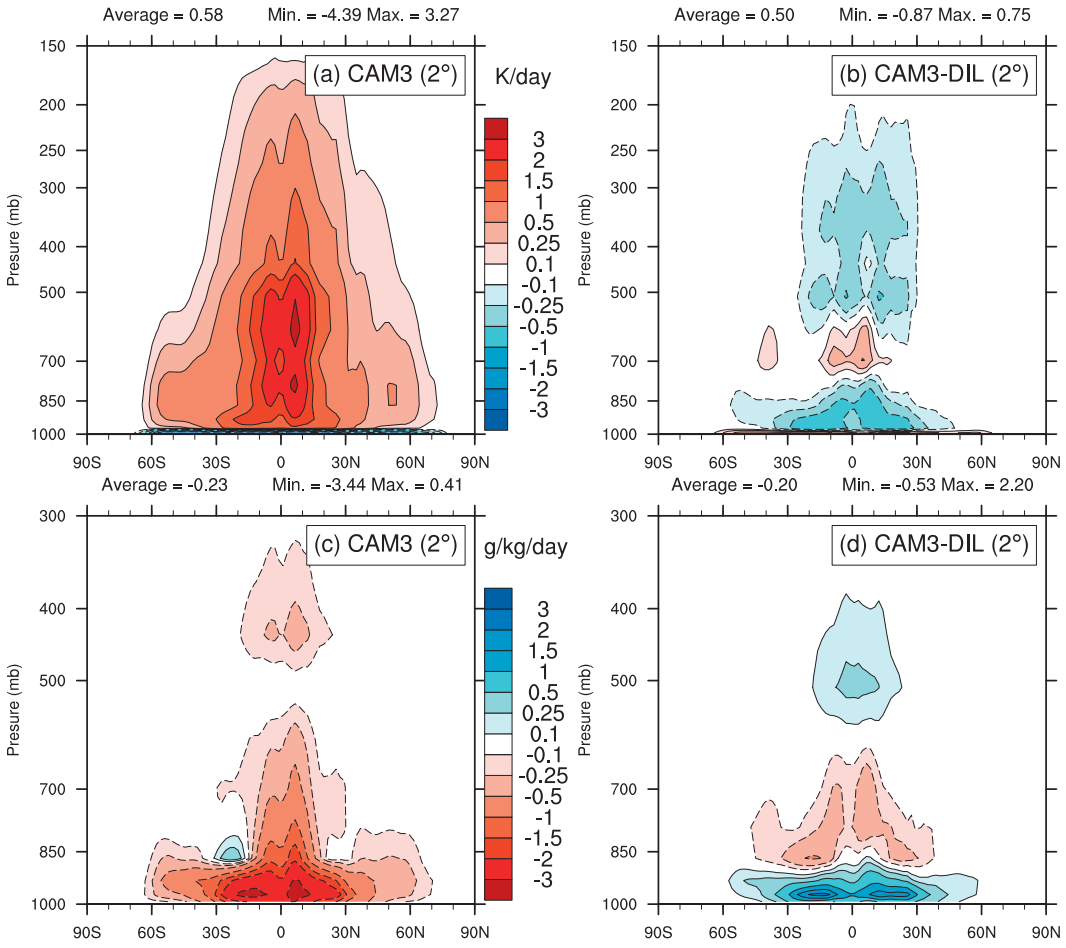

FIG. 5. Zonal and annually averaged deep convection tendencies in CAM3 at 2° for (a) temperature (K day^{-1}) and (c) specific humidity (g kg^{-1} day^{-1}). Deep convection tendencies in CAM3-DIL minus CAM3 for (b) temperature and (d) specific humidity.

d. Freeze drying, cloud fraction, and cloud radiative forcing

The application of the new convection changes, the inclusion of freeze-drying processes, and the improved equilibrium cloud state all lead to changes in the latitudinal distribution of cloud fraction and associated cloud radiative forcings. Figure 6 shows significant decreases in both total and low cloud fraction from CAM3 to CAM4. The most significant decreases are over Northern Hemisphere mid- to high-latitude regions in the transition from CAM3-DIL to CAM3.5 model versions. The differences can be attributed to the freeze drying, which dominates Arctic low cloud in wintertime, and the improved cloud equilibrium state, which dominates changes in midlatitudes. The implementation of freeze drying was motivated by the observed excess of low cloud as seen in surface-based observations and satellite measurements (including ISCCP). *CloudSat* observations were only available later in the period and indicated the excess in polar low cloud was not as severe. Cloud reductions in CAM4 within the tropics and subtropics are much lower than at higher latitudes. The inclusion of DCAPE appears to account for most of this reduction (although the response is largely a vertical redistribution) with a further minor reduction from the new equilibrium cloud fraction calculation in CAM3.5. There does, however, appear to be significant dependencies of cloud fraction on model resolution. In CAM3 T85 has systematically less cloud than T42 in the extratropics and polar regions. In addition, the switch to the 2° FV core in CAM3 changes the character of cloud evolution with latitude such that amounts look similar to T85 in midlatitudes, but then transition to looking more like the T42 resolution near the poles. A similar sensitivity to resolution also appears in CAM4 with a somewhat larger signal in the tropics in total cloud. This is to some extent related to a greater retention of cloud water

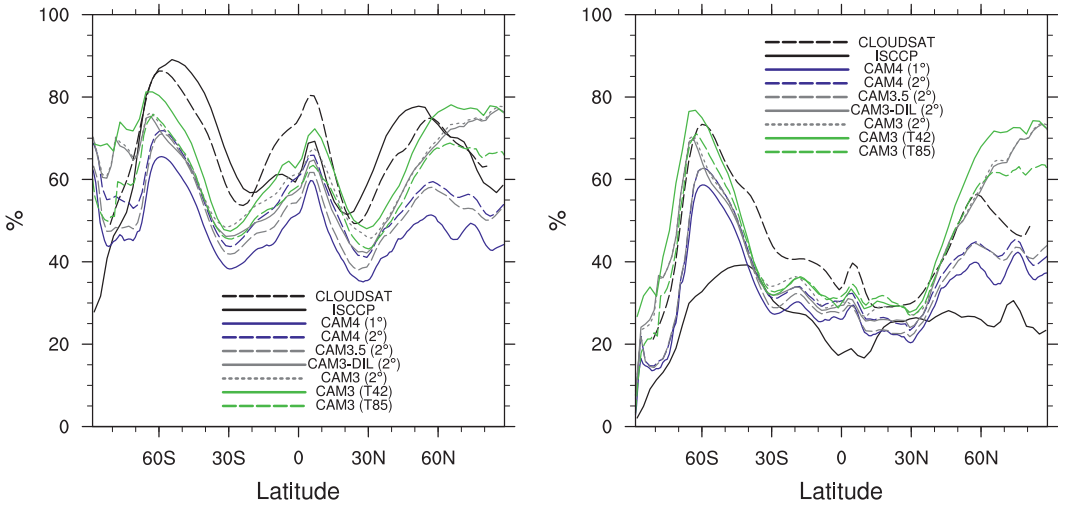

FIG. 6. Zonally averaged distribution of cloud fraction (%) from observations, and CAM3 and CAM4 simulations. (left) Total cloud and (right) low cloud below approximately 700 hPa. Observed datasets are from *CloudSat* and ISCCP.

in CAM4 at 2° because of the reduction in the fall velocity of ice particles compared to CAM4 at 1°.

The reduction in cloud amount at most levels in the atmosphere also impacts the latitudinal distribution of cloud radiative forcing. During the development of CAM4 more emphasis was progressively placed on validation using the CERES-EBAF (Loeb et al. 2009) cloud radiative products rather than the ERBE (Barkstrom and Hall 1982) products used to validate CAM3 climates. This was primarily a result of the energy balanced characteristics of CERES-EBAF that made it more suitable for the near balanced energetics of the earth system. Figure 7 shows the combined impact of the cloud fraction, cloud macrophysical and microphysical changes between CAM3 and CAM4. The shortwave cloud-radiative forcing (SWCF) changes are primarily in response to low- and midlevel cloud fraction reductions. The decreases in SWCF tend to be an improvement in the Northern Hemisphere and a slight degradation in the Southern Hemisphere storm-track regions compared to CAM3. Consistent with the low-cloud fraction decrease the largest contribution comes from the improved equilibrium cloud fraction calculation in addition to a systematic sensitivity to increased horizontal resolution. In the tropics, CAM continues to systematically overestimate SWCF and this was moderately

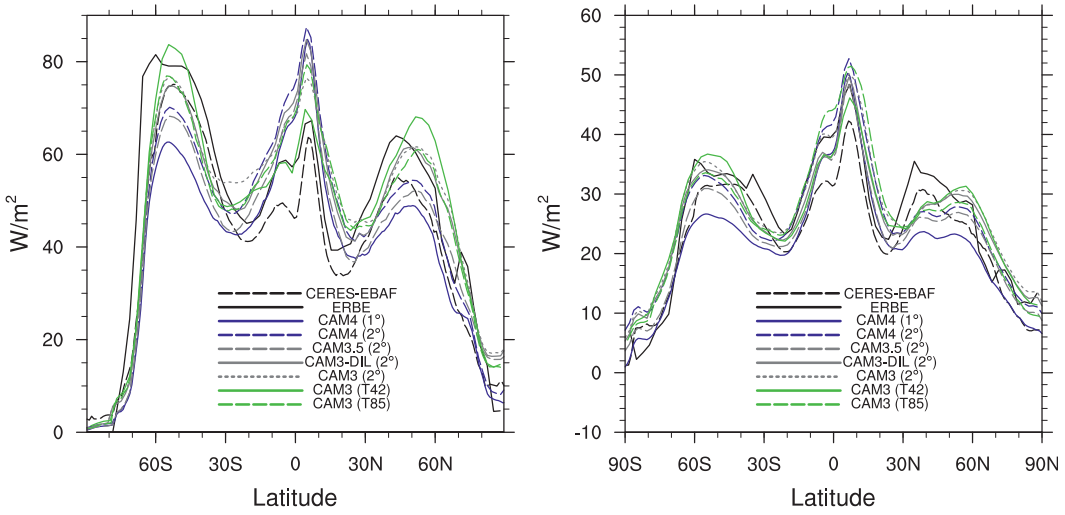

FIG. 7. Zonally averaged distribution of cloud radiative forcing (W m^{-2}) from observations, and CAM3 and CAM4 simulations. (left) SWCF (positive represents cooling) and (right) LWCF (positive represents warming).

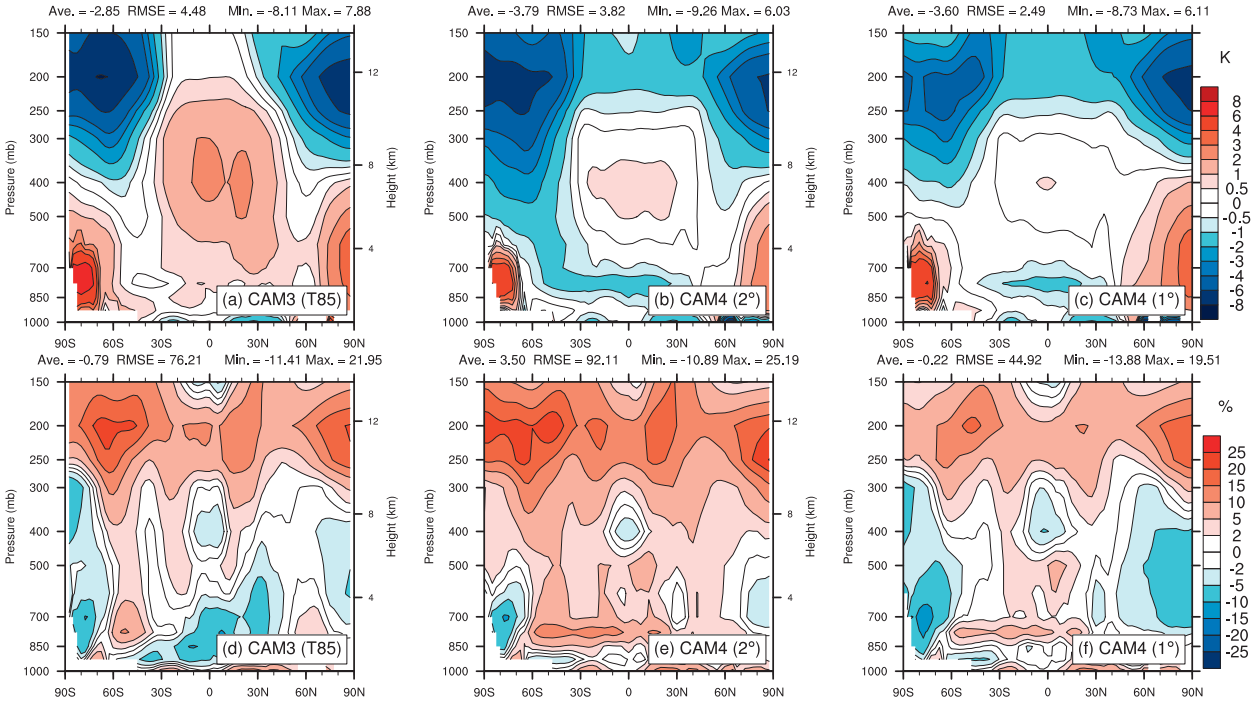

FIG. 8. (top) Zonal and annually averaged temperature biases (K) and (bottom) relative humidity biases for (a),(d) CAM3 at T85, (b),(e) CAM4 at 2°, and (c),(f) CAM4 at 1° compared to ERA-40.

exacerbated by the increased midlevel detrainment and formation of cloud with the inclusion of DCAPE. Although increased resolution plays a role in increasing tropical SWCF in CAM3, this sensitivity is significantly lower in CAM4. The longwave cloud forcing (LWCF) changes largely offset those seen in SWCF, which explains why climates that are nearly energy balanced are possible with most of the CAM configurations shown here. CAM3.5 simulations reveal a moderate drop in LWCF in the midlatitude storm tracks. More concerning is the significant sensitivity of LWCF to resolution seen in CAM4 in these regions. Even though CERES-EBAF estimates are lower than ERBE the CAM4 1° simulations are lower still and begin to smear out the local storm-track maxima, particularly in the Northern Hemisphere. In the tropics, LWCF continues to be overestimated in CAM4 which is a reflection of the continued presence of a double ITCZ, the details of which are in the next section.

Although CAM4 suffers from some degradation in cloud the extensive physics parameterization developments in the model's successor CAM5 provides a much improved simulation of cloud and cloud optical properties, particularly when analyzed through the Cloud Observation Simulator Package (COSP) diagnostics available in CAM (Kay et al. 2012). There is also a significantly lower sensitivity in cloud radiative forcing to increasing resolution (J. Bacmeister 2013, unpublished manuscript).

5. Climate simulation impact changes

The changes to mean climate and climate variability in CAM4 retain many of the changes seen in CAM3.5 and documented in Gent et al. (2011). As shown in the previous section, changes in aspects of the mean climate between CAM3 and CAM4 are attributable to changes associated with dynamical core, moderate physical parameterization changes, and horizontal resolution. In this section we will document major changes in the regional climate comparing not only CAM3 and CAM4 AMIP type experiments, but also a subset of experiments with a fully interactive coupled ocean as previously documented in Gent et al. (2011) and Collins et al. (2006b) and whose details are documented in Table 1. Tropospheric distributions in specific humidity and temperature are generally improved in CAM4 (Fig. 8). Tropical upper-tropospheric reductions in warm temperature biases are largely as a result of the restricted ability of ZM to overstabilize the temperature profile because of DCAPE. Similarly, upper-tropospheric humidity errors are decreased because of a reduced response from ZM. Lower-tropospheric tropical relative humidity deficits in CAM3 are replaced by slight moist anomalies in response to the deepening of the boundary layer from including DCAPE as it inherently results in greater mixing in the lower troposphere. The significant reduction in midlatitude

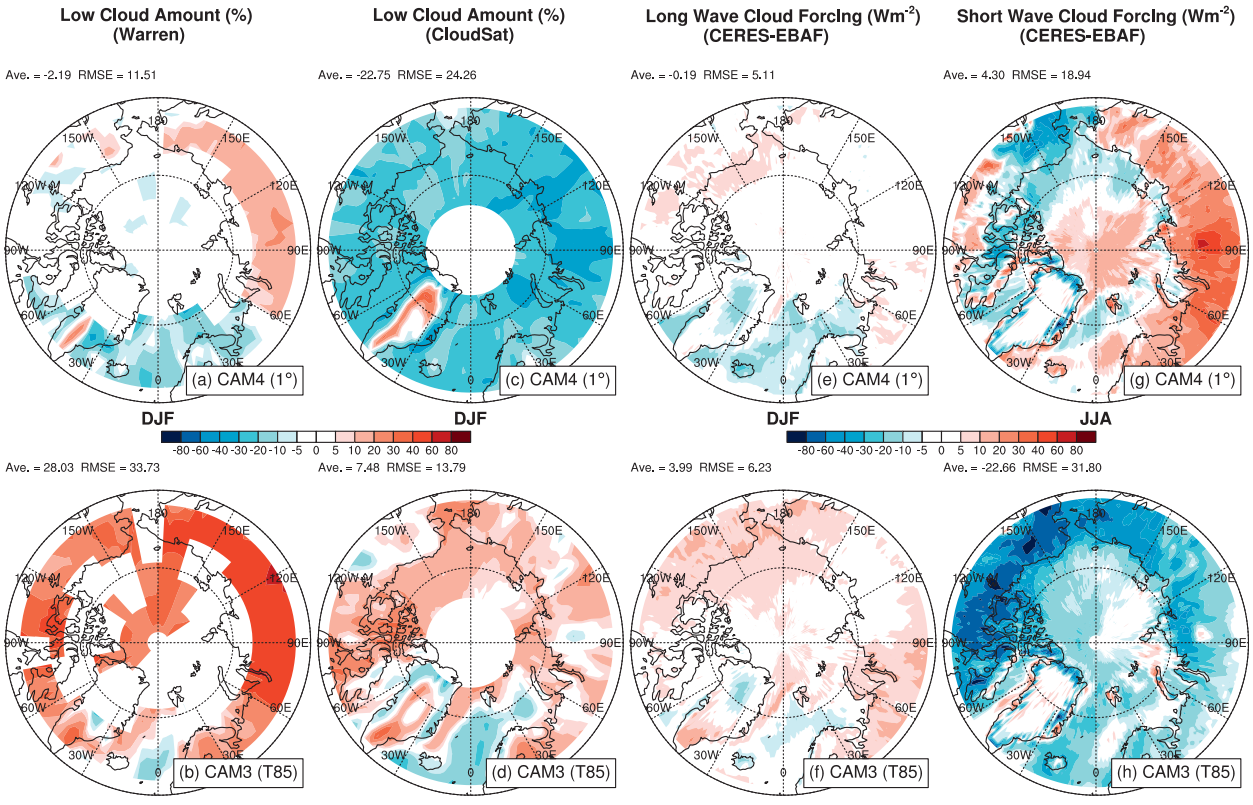

FIG. 9. Polar low-cloud bias in CAM3 at T85 and CAM4 at 1° for DJF integrated low cloud (surface to 700 hPa) compared to (a),(b) WARREN in situ observations, (c),(d) *CloudSat*-based observations, (e),(f) DJF LWCF, and (g),(h) JJA SWCF; all compared to the CERES-EBAF equivalent cloud forcing products.

LWCF at high resolution in CAM4 at 1° is also reflected in an increase in tropospheric temperature from 60° poleward, further exacerbating minor low relative humidity biases seen in CAM4 at 2°. Given the relative humidity closure of the Zhang et al. (2003) scheme in CAM, it is no surprise this reduces the LWCF of middle to high clouds in these regions. The cold-pole problem is largely retained even with the change to the FV core, but with some suggestion the problem is reduced in the Southern Hemisphere in CAM4 at 1°.

A further reflection of regional differences between CAM3 and CAM4 is seen in the polar cloud differences (Fig. 9). In CAM3 wintertime polar cloud amount was observed to be elevated by as much as 50% when compared with WARREN and ISCCP (not shown) low cloud amount. This prompted the inclusion of the freeze-drying approximation (Vavrus and Waliser 2008) which reduces high-latitude and polar cloud fraction in the presence of low water vapor values in CAM4. Although it became apparent later with the availability of the *CloudSat* observations that low cloud fractions were not as excessive in CAM3 as originally thought, the freeze drying does have a positive impact on the excessive continental LWCF and combined with other cloud changes, yields an improvement in the excessive summertime SWCF. Furthermore, over many areas low cloud fraction is now actually less than observed when comparing CAM4 and *CloudSat*.

Although there are significant documented improvements in the transient behavior of both the CAM4 atmosphere [e.g., the MJO; Subramanian et al. (2011)] and CCSM4 fully coupled system [e.g., ENSO; Deser et al. (2012)], many of the errors associated with the ITCZ remain (Fig. 10). In AMIP-type experiments CAM4 continues to overestimate the magnitude of tropical precipitation and maintains a significant double ITCZ. This is the case when compared to TRMM and particularly true when compared against GPCP where evidence of significant tropical underestimation continues to mount (Onogi et al. 2011). CAM4 worsens the northern ITCZ branch, especially at the higher 1° resolution. This is consistent with the excessive trades and associated increased low-level moisture supply identified earlier as a result of the change to the FV dynamical core. In fully coupled experiments, as with CCSM3, Northern Hemisphere ITCZ biases are reduced significantly in CCSM4,

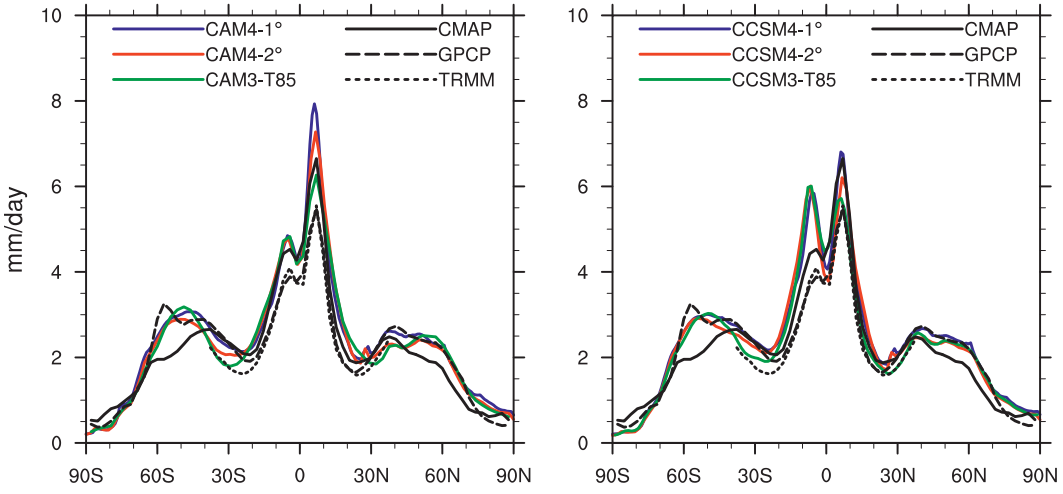

FIG. 10. Zonal and annually averaged mean precipitation (mm day^{-1}) for (left) AMIP-type CAM experiments and (right) fully coupled CCSM experiments compared to CMAP (1979–98), GPCP (1979–2003), and TRMM (1998–2004) observations.

especially when compared to CMAP. Consistent with all observations, CCSM4 also retains a larger Northern Hemisphere precipitation maximum compared to the Southern Hemisphere maximum, although the maximum is reduced compared to CAM4 simulations, ameliorating the impact of the increased trade winds. This was not the case in CCSM3. Although zonally averaged precipitation improvements in CAM4 and CCSM4 are marginal at best, the regional distribution of bias reductions is much more significant. In Fig. 11 AMIP-type experiments show marginal improvements in global RMSE in CAM4 simulations, and it is clear that global improvements are hindered by a worsening of the northern branch of the ITCZ in the central and eastern Pacific. However, regional improvements in precipitation are evident in CAM4, particularly at 1°. These include a decrease in the excessive Indian monsoon rainfall and a reduction in the Northern Hemisphere western ocean basin rainfall deficits associated with improved resolution of baroclinic storm activity in CAM4 1° simulations. The benefits of CAM4 being coupled to the updated version of POP are also illustrated in Fig. 11. Even though the global mean bias in precipitation increases, the RMSE is reduced in CCSM4 compared to CCSM3, so much so that the simulation skill in CCSM4 at 1° is equivalent to CAM4 at 1°. These global improvements come largely from a reduction in the southern ITCZ bias and west Indian Ocean errors seen in CCSM3.

For the fully coupled climate, surface stresses are the primary driver of the dynamic circulation. In this respect CAM4 and in particular CCSM4 show significant improvements compared to CAM3 and CCSM3. Figure 12 shows the surface zonal stress anomalies of AMIP-type and fully coupled experiments. CAM3 produced a very strong Southern Hemisphere westerly surface stress approximately 50% greater than observed. This bias translates to the CCSM3 simulations and also worsens. The oceanic consequences are an associated excessive Antarctic Circumpolar Current (ACC) and too much transport through the Drake Passage (Large and Danabasoglu 2006). In CAM4 and CCSM4 these Southern Ocean zonal surface stresses are improved markedly, particularly in CAM4. Coupling with an interactive ocean increases the biases proportionately more than in CCSM3, but biases remain significantly lower, particularly in the Indian and west Pacific Oceans. A potential mechanism for the improvement in the Southern Ocean surface stress is a shift and correction in the teleconnections associated with Northern Hemisphere summertime tropical heating patterns. Figure 13 shows June–August (JJA) averaged upper-tropospheric velocity potential and streamfunction, broadly representing tropical heating and barotropic teleconnection responses respectively (Sardeshmukh and Hoskins 1987). During JJA the Asian monsoon dominates the tropical heating and upper-tropospheric divergent flow. Vorticity advection of the divergent flow establishes the stationary Rossby wave response with a pair of cyclones to the west of the maximum divergence. Both CAM3 and CAM4 overestimate the upper-tropospheric divergent flow with local velocity potential maxima near the Arabian Peninsula. Since the excess is slightly larger in CAM3 because of large precipitation biases (see Fig. 11) it generates a larger anomalous Rossby wave response, particularly over the Indian subcontinent and in the

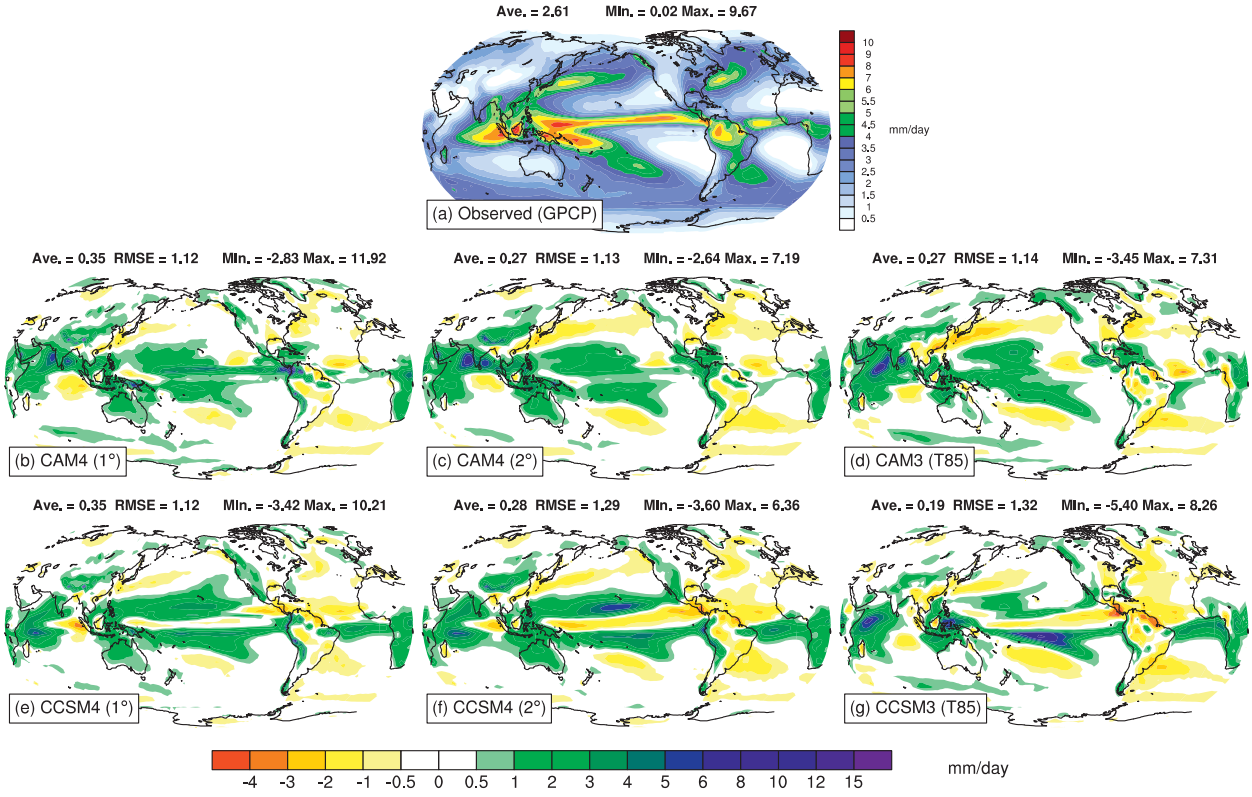

FIG. 11. Annually averaged (a) observed precipitation from GPCP (1979–2003) and model precipitation biases (mm day^{-1}) in AMIP-type experiments for (b) CAM4 at 1°, (c) CAM4 at 2°, and (d) CAM3 at T85, and in fully coupled experiments for (e) CCSM4 at 1°, (f) CCSM4 at 2°, and (g) CCSM3 at T85.

southern Indian Ocean. In the fully coupled equivalent analysis the divergent anomalies are much lower, reflecting an improved monsoon strength, but the streamfunction anomalies to the east of the heating anomalies have the potential to force a stronger anomalous barotropic response in the southern Indian Ocean and to the south of Australia, the regions with the largest positive zonal surface stress anomalies in CAM3 and CCSM3.

Atmospheric blocking and skill scores

Recent observed extreme weather events have been linked to persistent continental high pressure blocking systems, both in summer [e.g., 2010 Russian heat wave; Dole et al. (2011)] and winter [e.g., 2010 winter in northwestern Europe; Cattiaux et al. (2010)]. For a model to reproduce these kinds of extreme events at any particular resolution, it has to establish sufficient skill at capturing the underlying large-scale patterns of persistence. Previous versions of CAM have been analyzed for their skill in producing realistic blocking characteristics in AMIP simulations (D'Andrea et al. 1998) based on the operational weather forecast blocking index of Tibaldi and Molteni (1990). Figure 14 shows the performance in CAM3 and CAM4 model configurations. Blocking statistics are somewhat variable from one year to the next and between ensemble members of the same experiment configuration. However, it is clear that the blocking behavior in CAM4 is significantly different and mostly superior to CAM3. In Northern Hemisphere spring CAM significantly underestimates Atlantic blocking by more than a factor of 2 in CAM3. Simulations using CAM4 are able to produce significantly increased blocking frequency over western Europe, but large deficiencies remain over the majority of the Atlantic sector. In fully coupled CCSM4 simulations Atlantic blocking deficiencies are even greater (not shown) because of significant Gulf Stream separation–related SST errors. Pacific blocking is also underestimated in CAM3 with a slight increase in frequency in CAM4. These minor improvements result from a change in the downstream stationary wave pattern in response to the changing tropical convective heat source. This also appears to be the case in summer where very low blocking frequencies in CAM3 are replaced with a more realistic double blocking peak in CAM4 near 130° and 30°E. Most of the blocking frequency

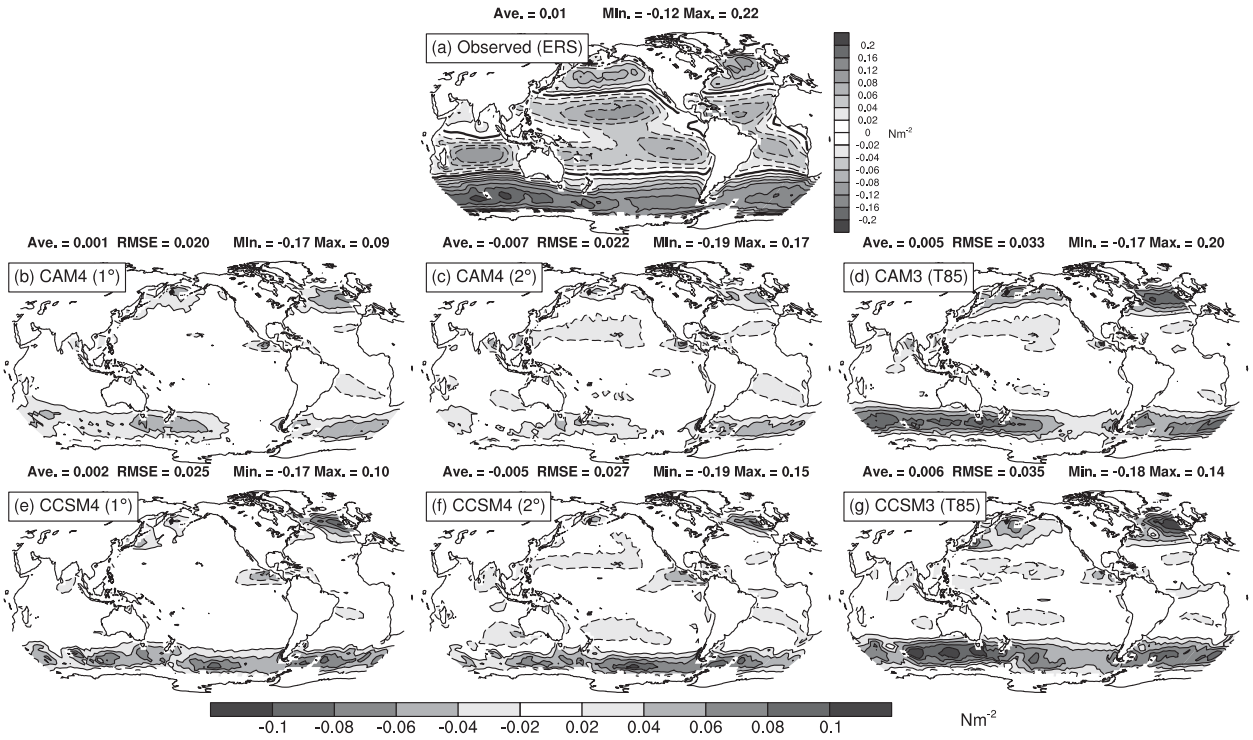

FIG. 12. As in Fig. 11, but for surface zonal stress (N m^{-2}) using ERS observations.

changes in CAM4 also occur independently of the dynamical core change to FV.

A final simulation performance measure for CAM4 is a set of simulation error scores based on the Northern Hemisphere wintertime average 200-hPa height field. These error scores have been documented and used in many previous versions of CAM and its predecessors (Collins et al. 2006a; Kiehl et al. 1998) to provide a stable measure of model improvement associated with the Northern Hemisphere wintertime stationary wave pattern. Figure 15 shows the normalized mean-square error (NMSE) and the scaled variance ratio (SVR) for CAM3, CAM4, and a number of development runs. Previous model versions were diagnosed just for January climatology (Fig. 15a), but a more robust test of model performance is presented for the whole DJF winter climatology (Fig. 15b). Briefly, SVR is a measure of how NMSE can be erroneously improved through higher model variance, and NMSE is a sum of the unconditional model bias $U(Z_m)$, the conditional model bias $C(Z_m)$, and a measure of phase error $P(Z_m)$, that goes to zero when model and analysis fields are perfectly correlated. For both January and DJF, error scores degrade upon initial inclusion of the FV core through a jump in the unconditional bias. However, through successive development versions of the model the unconditional bias is reduced, most prominently in response to both the CMT and DCAPE changes in the CAM3-CONV simulation. For the whole DJF climatology the error score then decreases monotonically with CAM3.5, CAM4 at 2°, and CAM4 at 1°. Clearly more effort was invested in providing a more accurate climate simulation for CAM3.5 and CAM4, but it is illustrative that not all changes to the model configuration result in a monotonic improvement in mean climate, at least using this error score. Additionally, although the error scores may have improved between CAM3 and CAM4, there is still much more similarity among all the reanalyses than between any one reanalysis and CAM4, implying that significant model errors remain.

6. Conclusions

This paper describes the evolution of the community atmosphere model (CAM) mean climate in development from versions CAM3 to CAM4 in both prescribed SST (AMIP) and fully coupled experiments. Major physics changes are the addition of a dilute CAPE (DCAPE) closure calculation and convective momentum transport (CMT) in the ZM deep convection scheme. Additional moist physics changes include a freeze-drying mechanism to alleviate winter polar cloud excesses and

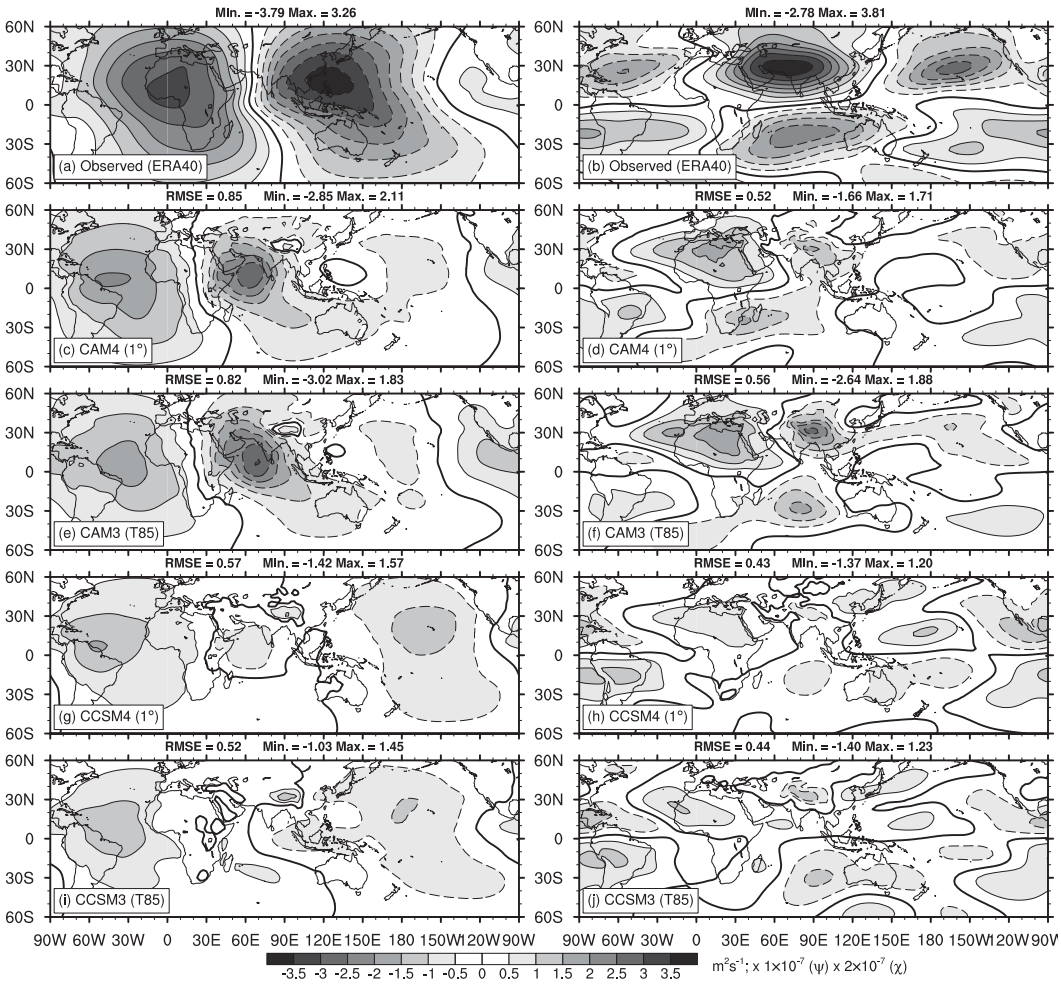

FIG. 13. (left) JJA average 150-hPa streamfunction ($m^2\ s^{-2}$) and (right) velocity potential ($m^2\ s^{-2}$) for (a),(b) ERA-40 and bias for (c),(d) CAM4 at 1°, (e),(f) CAM3 at T85, (g),(h) CCSM4 at 1°, and (i),(j) CCSM3 at T85.

a more consistent calculation of cloud fraction that passes a thermodynamic state to the radiation calculation that is much closer to macrophysical equilibrium. Although simulations using CAM4 improve significantly on CAM3, mostly in the area of transient variability (e.g., Subramanian et al. 2011; Deser et al. 2012), there are also significant improvements in the mean climate. Chief among these are the improvements in tropical precipitation distributions, tropospheric humidity distributions, wintertime polar cloud amounts, and surface stress distributions. The reduction in excessive surface stresses has had a more noticeable impact on the fully coupled climate. In the tropical Pacific improvements resulting from CMT have been implicated in the associated CCSM4 ENSO improvements (Neale et al. 2008) and the reductions in Southern Hemisphere surface stresses have reduced the strength of the associated ACC and Drake Passage transport (Large and Danabasoglu 2006). There are, however, only marginal improvements and some degradation in the zonal-mean cloud-related quantities in CAM4. Outside of the wintertime arctic cloud changes, the modifications to the moist physics (DCAPE and the equilibrium cloud fraction calculation) were not intended to address specific simulation shortcomings in cloud fraction and radiative properties. As a consequence, cloud and cloud forcing has decreased in the extratropics, which on the whole is in poorer agreement with observations. This disagreement is exacerbated with CAM4 at 1°, indicating a sensitivity to horizontal resolution, but which is much lower than in CAM3 using the spectral dynamical core. Initial results show that the CAM4 resolution sensitivity is much more acute in 0.25° simulations (Bacmeister 2013, unpublished manuscript) and it has not been possible to correct for these biases in the current physics framework. Developments toward version 5 of CAM (CAM5; Rasch et al.

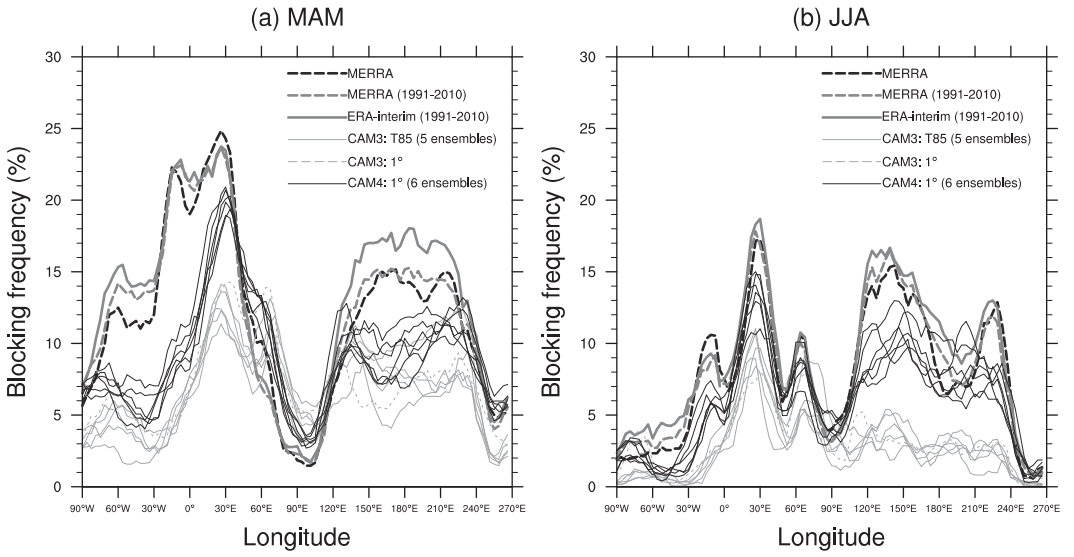

FIG. 14. Longitudinal Northern Hemisphere blocking frequency as determined by the blocking index of D'Andrea et al. (1998) for reanalyses and, CAM3 and CAM4 ensemble experiments during (a) March–May (MAM) and (b) JJA for the time period 1981–2000, unless otherwise stated.

2013, unpublished manuscript) reduce some of the cloud-resolution sensitivities significantly. This is in large part a result of the shift in ice cloud closure from a purely relative humidity based formulation in CAM3 and CAM4 (Zhang et al. 2003) to a scheme that allows ice supersaturation (Gettelman et al. 2010) when working in concert with the new CAM5 two-moment microphysics (Morrison and Gettelman 2008).

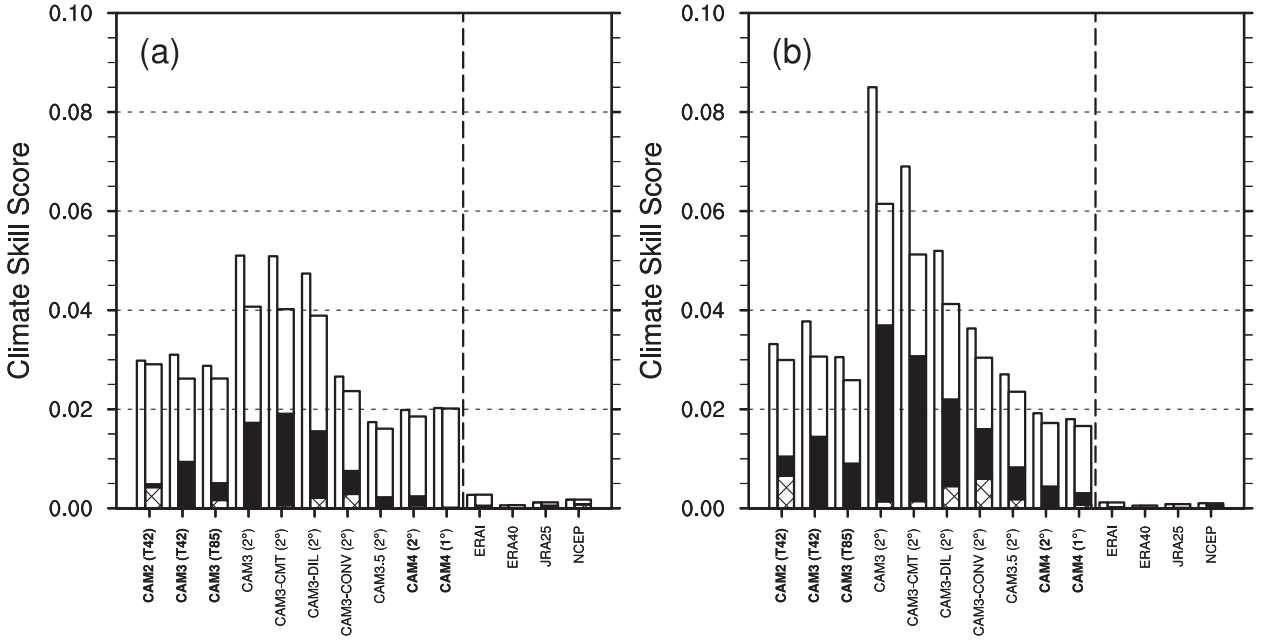

FIG. 15. Error score measures of NMSE and SVR for CAM versions described in Table 1 (release versions in boldface) as compared with ERA-15 (Gibson et al. 1997) for (a) January and (b) DJF climatologies. SVR is the thin white bar on the left of each pair of bars and NMSE is on the right shown as the sum of the terms $U(z_m)$ (hatched), $C(Z_m)$ (black), and $P(Z_m)$ (white). All measures are described in the text. For comparison, error scores for alternate reanalysis products ERA-Interim, ERA-40, JRA-25, and NCEP are to the right of the vertical dashed line.

Acknowledgments. The CESM project is supported by the National Science Foundation and the U.S. Department of Energy Office of Science Biological and Environmental Research (BER) program. The National Center for Atmospheric Research is sponsored by the National Science Foundation. Thanks are also due to the many other software engineers and scientists who worked on developing CAM4 and CCSM4. Computing resources were provided by the Climate Simulation Laboratory at NCAR's Computational and Information Systems Laboratory (CISL), sponsored by the National Science Foundation and other agencies. This research was enabled by CISL compute and storage resources. Bluefire, a 4064-processor IBM Power6 resource with a peak of 77 teraFLOPS, provided more than 7.5 million computing hours, the GLADE high-speed disk resources provided 0.4 petabytes of dedicated disk, and CISL's 12-PB HPSS archive provided over 1 petabyte of storage in support of this research project.

REFERENCES

Adler, R. F., and Coauthors, 2003: The version-2 Global Precipitation Climatology Project (GPCP) monthly precipitation analysis (1979–present). *J. Hydrometeor.,* **4,** 1147–1167.

Attema, E. P. W., 1991: The Active Microwave Instrument onboard the ERS-1 Satellite. *Proc. IEEE,* **76,** 791–799.

Barkstrom, B. R., and J. B. Hall, 1982: Earth Radiation Budget Experiment (ERBE)—An overview. *J. Energy,* **6,** 141–146.

Cattiaux, J., R. Vautard, C. Cassou, P. Yiou, V. Masson-Delmotte, and F. Codron, 2010: Winter 2010 in Europe: A cold extreme in a warming climate. *Geophys. Res. Lett.,* **37,** L20704, doi:10.1029/2010GL044613.

Collins, W. D., P. J. Rasch, B. A. Boville, J. J. Hack, J. R. McCaa, D. L. Williamson, and B. P. Briegleb, 2006a: The formulation and atmospheric simulation of the Community Atmosphere Model version 3 (CAM3). *J. Climate,* **19,** 2144–2161.

——, and Coauthors, 2006b: The Community Climate System Model version 3 (CCSM3). *J. Climate,* **19,** 2122–2143.

Dai, A., 2006: Precipitation characteristics in eighteen coupled climate models. *J. Climate,* **19,** 4605–4630.

D'Andrea, F., and Coauthors, 1998: Northern Hemisphere atmospheric blocking as simulated by 15 atmospheric general circulation models in the period 1979–1988. *Climate Dyn.,* **14,** 385–407.

Dee, D. P., and Coauthors, 2011: The ERA-Interim Reanalysis: Configuration and performance of the data assimilation system. *Quart. J. Roy. Meteor. Soc.,* **137,** 553–597.

Dennis, J., and Coauthors, 2012: CAM-SE: A scalable spectral element dynamical core for the Community Atmosphere Model. *Int. J. High Perform. Comput. Appl.,* **26,** 74–89, doi:10.1177/1094342011428142.

Deser, C., and Coauthors, 2012: ENSO and Pacific decadal variability in Community Climate System Model version 4. *J. Climate,* **25,** 2622–2651.

Dole, R., and Coauthors, 2011: Was there a basis for anticipating the 2010 Russian heat wave? *Geophys. Res. Lett.,* **38,** L06702, doi:10.1029/2010GL046582.

Emmons, L. K., and Coauthors, 2009: Description and evaluation of the Model for Ozone and Related Chemical Tracers, version 4 (MOZART-4). *Geosci. Model Dev. Discuss.,* **2,** 1157–1213, doi:10.5194/gmdd-2-1157-2009.

Evans, K., P. H. Lauritzen, S. Mishra, R. B. Neale, M. A. Taylor, and J. J. Tribbia, 2013: AMIP simulation with the CAM4 spectral element dynamical core. *J. Climate,* **26,** 689–709.

Gent, P. R., S. G. Yeager, R. B. Neale, S. Levis, and D. A. Bailey, 2010: Improvements in a half degree atmosphere/land version of the CCSM. *Climate Dyn.,* **34,** 819–833, doi:10.1007/s00382-009-0614-8.

——, and Coauthors, 2011: The Community Climate System Model version 4. *J. Climate,* **24,** 4973–4991.

Gettelman, A., and Coauthors, 2010: Global simulations of ice nucleation and ice supersaturation with an improved cloud scheme in the Community Atmosphere Model. *J. Geophys. Res.,* **115,** D18216, doi:10.1029/2009JD013797.

Gibson, J. K., P. Kallberg, S. Uppala, A. Noumura, A. Hernandez, and E. Serrano, 1997: ECMWF Re-Analysis Project report series: ERA description. ECMWF Tech. Rep. 1, 77 pp.

Gregory, D., R. Kershaw, and P. M. Inness, 1997: Parametrization of momentum transport by convection. II: Tests in single-column and general circulation models. *Quart. J. Roy. Meteor. Soc.,* **123,** 1153–1183.

Hahn, C. J., and S. G. Warren, 2007: A gridded climatology of clouds over land (1971–96) and ocean (1954–97) from surface observations worldwide. Carbon Dioxide Information Analysis Center Tech. Rep. NDP-026E, 71 pp.

Huffman, G. J., and Coauthors, 2007: The TRMM Multisatellite Precipitation Analysis (TMPA): Quasi-global, multiyear, combined-sensor precipitation estimates at fine scales. *J. Hydrometeor.,* **8,** 38–55.

Kanamitsu, M., W. Ebisuzaki, J. Woollen, S.-K. Yang, J. J. Hnilo, M. Fiorino, and G. L. Potter, 2002: NCEP–DOE AMIP-II Reanalysis (R-2). *Bull. Amer. Meteor. Soc.,* **83,** 1631–1643.

Kay, J. E., and A. Gettelman, 2009: Cloud influence on and response to seasonal arctic sea ice loss. *J. Geophys. Res.,* **114,** D18204, doi:10.1029/2009JD011773.

——, and Coauthors, 2012: Exposing global cloud biases in the Community Atmosphere Model (CAM) using satellite observations and their corresponding instrument simulators. *J. Climate,* **25,** 5190–5207.

Kershaw, R., and D. Gregory, 1997: Parametrization of momentum transport by convection. I: Theory and cloud modelling results. *Quart. J. Roy. Meteor. Soc.,* **123,** 1133–1151.

Kiehl, J. T., J. J. Hack, G. B. Bonan, B. B. Boville, D. L. Williamson, and P. J. Rasch, 1998: The National Center for Atmospheric Research Community Climate Model: CCM3. *J. Climate,* **11,** 1131–1149.

Kopp, G., and J. L. Lean, 2011: A new, lower value of total solar irradiance: Evidence and climate significance. *Geophys. Res. Lett.,* **38,** L01706, doi:10.1029/2010GL045777.

Lamarque, J.-F., and Coauthors, 2010: Historical (1850–2000) gridded anthropogenic and biomass burning emissions of reactive gases and aerosols: Methodology and application. *Atmos. Chem. Phys.,* **10,** 7017–7039.

——, and Coauthors, 2012: CAM-chem: Description and evaluation of interactive atmospheric chemistry in the Community Earth System Model. *Geosci. Model Dev.,* **5,** 369–411, doi:10.5194/gmd-5-369-2012.

Large, W. G., and G. Danabasoglu, 2006: Attribution and impacts of upper-ocean biases in CCSM3. *J. Climate,* **19,** 2335–2346.

Lauritzen, P. H., C. J. M. Taylor, and R. D. Nair, 2010: Rotated versions of the Jablonowski steady-state and baroclinic wave

test cases: A dynamical core intercomparison. *J. Adv. Model. Earth Syst.,* **2,** 34 pp. [Available online at http://onlinelibrary.wiley.com/doi/10.3894/JAMES.2010.2.15/pdf.]

——, A. T. Mirin, J. E. Truesdale, K. Raeder, J. L. Anderson, J. Bacmeister, and R. B. Neale, 2011: Implementation of new diffusion/filtering operators in the CAM-FV dynamical core. *Int. J. High Perform. Comput. Appl.,* **123,** 1133–1151, doi:10.1177/1094342011410088.

Lin, S. J., 2004: A ''vertically Lagrangian'' finite-volume dynamical core for global models. *Mon. Wea. Rev.,* **132,** 2293–2307.

——, and R. B. Rood, 1996: Multidimensional flux-form semi-Lagrangian transport schemes. *Mon. Wea. Rev.,* **124,** 2406–2070.

Loeb, N. G., B. A. Wielicki, D. R. Doelling, G. L. Smith, D. F. Keyes, S. Kato, N. Manalo-Smith, and T. Wong, 2009: Toward optimal closure of the earth's top-of-atmosphere radiation budget. *J. Climate,* **22,** 748–766.

Mishra, S. K., M. A. Taylor, R. D. Nair, P. H. Lauritzen, H. M. Tufo, and J. J. Tribbia, 2011: Evaluation of the HOMME dynamical core in the aquaplanet configuration of NCAR CAM4: Rainfall. *J. Climate,* **24,** 4037–4055.

Morrison, H., and A. Gettelman, 2008: A new two-moment bulk stratiform cloud microphysics scheme in the NCAR Community Atmosphere Model (CAM3). Part I: Description and numerical tests. *J. Climate,* **21,** 3642–3659.

Neale, R. B., J. H. Richter, and M. Jochum, 2008: The impact of convection on ENSO: From a delayed oscillator to a series of events. *J. Climate,* **21,** 5904–5924.

——, and Coauthors, 2011: Description of the NCAR Community Atmosphere Model (CAM4). NCAR Tech. Note NCAR/TN-485+STR, 120 pp.

Onogi, K., and Coauthors, 2007: The JRA-25 Reanalysis. *J. Meteor. Soc. Japan,* **85,** 369–432.

——, and Coauthors, 2011: Improvements of top-of-atmosphere and surface irradiance computations with CALIPSO-, CloudSat-, and MODIS-derived cloud and aerosol properties. *J. Geophys. Res.,* **116,** D19209, doi:10.1029/2011JD016050.

Peterson, T. C., and R. S. Vose, 1997: An overview of the Global Historical Climatology Network temperature database. *Bull. Amer. Meteor. Soc.,* **78,** 2837–2849.

Rasch, P. J., D. B. Coleman, N. Mahowald, D. L. Williamson, S. J. Lin, B. A. Boville, and P. Hess, 2006: Characteristics of atmospheric transport using three numerical formulations for atmospheric dynamics in a single GCM framework. *J. Climate,* **19,** 2243–2266.

Raymond, D. J., and A. M. Blyth, 1986: A stochastic mixing model for non-precipitating cumulus clouds. *J. Atmos. Sci.,* **43,** 2708–2718.

——, and ——, 1992: Extension of the stochastic mixing model to cumulonimbus clouds. *J. Atmos. Sci.,* **49,** 1968–1983.

Richter, J. H., and P. J. Rasch, 2008: Effects of convective momentum transport on the atmospheric circulation in the Community Atmosphere Model, version 3. *J. Climate,* **21,** 1487–1499.

Rienecker, M. R., and Coauthors, 2011: MERRA: NASA's Modern-Era Retrospective Analysis for Research and Applications. *J. Climate,* **24,** 3624–3648.

Sardeshmukh, P. D., and B. J. Hoskins, 1987: On the derivation of the divergent flow from the rotational flow: The χ problem. *Quart. J. Roy. Meteor. Soc.,* **113,** 339–360, doi:10.1002/qj.49711347519.

Schiffer, R. A., and W. B. Rossow, 1983: The International Satellite Cloud Climatology Project (ISCCP): The first project of the World Climate Research Program. *Bull. Amer. Meteor. Soc.,* **64,** 779–784.

Subramanian, A. C., M. Jochum, A. J. Miller, R. B. Neale, and D. E. Waliser, 2011: The Madden–Julian oscillation in CCSM4. *J. Climate,* **24,** 6261–6282.

Taylor, K. E., D. Williamson, and F. Zwiers, cited 2001: AMIP II sea surface temperature and sea ice concentration boundary conditions. [Available online at http://www-pcmdi.llnl.gov/projects/amip/AMIP2EXPDSN/BCS/amip2bcs.php.]

Tibaldi, S., and F. Molteni, 1990: On the operational predictability of blocking. *Tellus,* **42A,** 343–365.

Uppala, S. M., and Coauthors, 2005: The ERA-40 Re-Analysis. *Quart. J. Roy. Meteor. Soc.,* **131,** 2961–3012.

Vavrus, S., and D. Waliser, 2008: An improved parameterization for simulating Arctic cloud amount in the CCSM3 climate model. *J. Climate,* **21,** 5673–5687.

Whitehead, J., C. Jablonowski, R. B. Rood, and P. H. Lauritzen, 2011: A stability analysis of divergence damping on a latitude–longitude grid. *Mon. Wea. Rev.,* **139,** 2976–2993.

Williamson, D. L., 2013: Dependence of APE simulations on vertical resolution with the Community Atmosphere Model, version 3. *J. Meteor. Soc. Japan,* in press.

——, and J. Olson, 2007: A comparison of forecast errors in CAM2 and CAM3 at the ARM Southern Great Plains site. *J. Climate,* **20,** 4572–4585.

Xie, P., and P. A. Arkin, 1997: Global precipitation: A 17-year monthly analysis based on gauge observations, satellite estimates, and numerical model outputs. *Bull. Amer. Meteor. Soc.,* **78,** 2539–2558.

Zhang, G. J., 2009: Effects of entrainment on convective available potential energy and closure assumptions in convection parameterization. *J. Geophys. Res.,* **114,** D07109, doi:10.1029/2008JD010976.

——, and N. A. McFarlane, 1995: Sensitivity of climate simulations to the parameterization of cumulus convection in the Canadian Climate Centre general circulation model. *Atmos.–Ocean,* **33,** 407–446.

Zhang, M., W. Lin, C. S. Bretherton, J. J. Hack, and P. J. Rasch, 2003: A modified formulation of fractional stratiform condensation rate in the NCAR Community Atmospheric Model (CAM2). *J. Geophys. Res.,* **108,** 4035, doi:10.1029/2002JD002523.